

Toolbox

Improved Plasmids for Fluorescent Protein Tagging of Microtubules in *Saccharomyces cerevisiae*

Steven M. Markus^{1,3†}, Safia Omer^{2†}, Kaitlyn Baranowski¹ and Wei-Lih Lee^{1,2*}

¹Biology Department, University of Massachusetts Amherst, 221 Morrill South, 611 North Pleasant Street, Amherst, MA 01003, USA

²Molecular and Cellular Biology Graduate Program, University of Massachusetts Amherst, 443 Morrill I North, 637 North Pleasant Street, Amherst, MA 01003, USA

³Current address: Biochemistry & Molecular Biology Department, Colorado State University, Fort Collins, CO 80523, USA

*Corresponding author: Wei-Lih Lee, wlee@bio.umass.edu

Abstract

The ability to fluorescently label microtubules in live cells has enabled numerous studies of motile and mitotic processes. Such studies are particularly useful in budding yeast owing to the ease with which they can be genetically manipulated and imaged by live cell fluorescence microscopy. Because of problems associated with fusing genes encoding fluorescent proteins (FPs) to the native α -tubulin (*TUB1*) gene, the FP-Tub1 fusion is generally integrated into the genome such that the endogenous *TUB1* locus is left intact. Although such modifications have no apparent consequences on cell viability, it is unknown if these genome-integrated FP-tubulin fusions negatively affect microtubule functions. Thus, a simple, economical and highly sensitive assay of microtubule function is required. Furthermore, the current plasmids available for generation of FP-Tub1 fusions have not kept pace with the

development of improved FPs. Here, we have developed a simple and sensitive assay of microtubule function that is sufficient to identify microtubule defects that were not apparent by fluorescence microscopy or cell growth assays. Using results obtained from this assay, we have engineered a new family of 30 FP-Tub1 plasmids that use various improved FPs and numerous selectable markers that upon genome integration have no apparent defect on microtubule function.

Keywords Bik1, Bim1, budding yeast, fluorescent proteins, microtubules, Tub1, tubulin

Received 20 October 2014, revised and accepted for publication 23 February 2015, uncorrected manuscript published online 25 February 2015

Cytoskeletal studies performed in the budding yeast *Saccharomyces cerevisiae* have revealed many crucial insights into phenomena that are well conserved in higher eukaryotic organisms. The genetic tractability of this organism combined with the ease with which they can be imaged by fluorescence microscopy makes them ideal and powerful tools for live cell studies. A key aspect of their utility is the ability to target specific regions of their genome for homologous recombination-mediated gene modification. For

instance, fluorescent tagging of endogenous genes allows for live cell fluorescence imaging of various cytoskeletal structures (1–4). Such techniques have revealed insights into processes ranging from endocytosis to cell division (5–9). In some cases, however, such as in the case of actin and tubulin, fluorescent tagging of endogenous genes can disrupt protein function, leading to cytoskeletal defects or even cell death (10). Thus, alternative strategies have been used over the years to tag such components. In the case of tubulin tagging, plasmids with fluorescent protein (FP)-Tub1 (α -tubulin) fusion cassettes are integrated into

[†]These authors contributed equally to this work.

the genome such that the endogenous *TUB1* open reading frame is left intact. Subsequent to *FP-TUB1* plasmid integration, the cells express two copies of *TUB1*: the native, untagged copy and a tagged version. Previous studies have shown this to be critical (11), as *FP-TUB1* does not complement a *TUB1* deletion, presumably because microtubules have a limited threshold of tolerance for lattice-incorporated FP-tagged tubulin (12). In most cases, because the cells remain viable following plasmid integration, it is not understood what function, if any, has been perturbed by the tagged FP.

Here, we set out to test the effects different integrated *FP-TUB1* plasmids have on microtubule function as judged by growth defects due to synthetic interaction with *bim1Δ* or *bik1Δ*. Although the choice of FP has little effect, we find that the site of plasmid integration can significantly contribute to growth defects. Our findings allowed us to develop a new family of *FP-TUB1* plasmids with a standard method for integration at the *TUB1* locus. To further improve the utility of these constructs, we utilized bright and photostable FPs that span the spectrum of fluorescent molecules, as well as mEos2, a green-to-red photoconvertible FP that is useful for protein dynamics studies. To expand their versatility, we combined each FP-Tub1 fusion with multiple selectable markers, thus offering a variety of options for fluorescence-based live cell imaging of microtubules.

Results and Discussion

Site-specific integration of an FP-Tub1 construct differentially affects microtubule function

Previous strategies to label microtubules in budding yeast have used homologous recombination to integrate a FP-Tub1-expressing plasmid into the *URA3* locus (9,13,14), *TRP1* locus (15), *LEU2* locus (16,17) or *TUB1* locus (18,19). In most experiments, site-specific targeting of a linearized FP-Tub1 plasmid is mediated by sequence homology between the plasmid-borne auxotrophic marker (e.g. *URA3*) and the respective chromosomal allele (e.g. *ura3-52*). One of the drawbacks of this strategy is that the choice of auxotrophic markers is limited to those that have the corresponding sequence in the host yeast strain. This limitation eliminates as options those markers for which the complete auxotrophic gene has been

deleted from the host strain (e.g. *his3Δ*, *leu2Δ* and *trp1Δ*), and also eliminates antibiotic resistant marker genes, which have no corresponding complementary sequence within the yeast genome (e.g. kanamycin and hygromycin resistance genes). Further complicating this approach is that different targeting strategies must be conceived for each different selectable marker-containing targeting plasmid. In contrast, targeting FP-Tub1 constructs to a single site – the *TUB1* locus – overcomes these problems, because the homologous sequence for recombination is within the *TUB1* gene. However, although this strategy has been used in various experiments, it is unknown if affecting the *TUB1* locus impacts microtubule function.

To address this question, we first generated yeast strains with a differentially targeted FP-Tub1 vector. The plasmid we chose (pRS306:*HIS3p:mCherry-TUB1*) (15) contains an *mCherry-TUB1* fusion under the control of the *HIS3* promoter (*HIS3p*) and a *URA3* selectable marker (Figure 1A). Upon digestion with *ApaI*, which cuts within the *URA3* gene, the exposed ends of the linearized plasmid would theoretically target the construct for integration into the *ura3-52* locus. Alternatively, we hypothesized that digestion within the *TUB1* sequence of the plasmid, using *BsaBI*, as pictured in Figure 1A, would target the plasmid for integration into the *TUB1* locus. After digesting with either *ApaI* or *BsaBI* and transforming into yeast, we prepared genomic DNA from clonal isolates expressing mCherry-labeled microtubules as confirmed by fluorescence microscopy. Using diagnostic polymerase chain reaction (PCR) primer pairs shown in Figure 1A and listed in Table 1, we confirmed that the plasmid was indeed differentially targeted to *ura3-52* and *TUB1* locus as a result of linearization with *ApaI* and *BsaBI*, respectively (Figure 1B).

Close inspection of the two yeast strains with the differentially targeted mCherry-Tub1 construct revealed no readily apparent difference in microtubule morphology or behavior (as assessed by fluorescence microscopy) or cell growth (not shown). To more carefully assess microtubule function in these cells, we performed a synthetic genetic analysis of the different *HIS3p:mCherry-TUB1* alleles with the microtubule-binding proteins, Bim1 and Bik1. Previous studies have shown that yeast strains deficient for *BIM1* (*bim1Δ*) or *BIK1* (*bik1Δ*) exhibit synthetic lethality with mutations in *TUB1* (20,21).

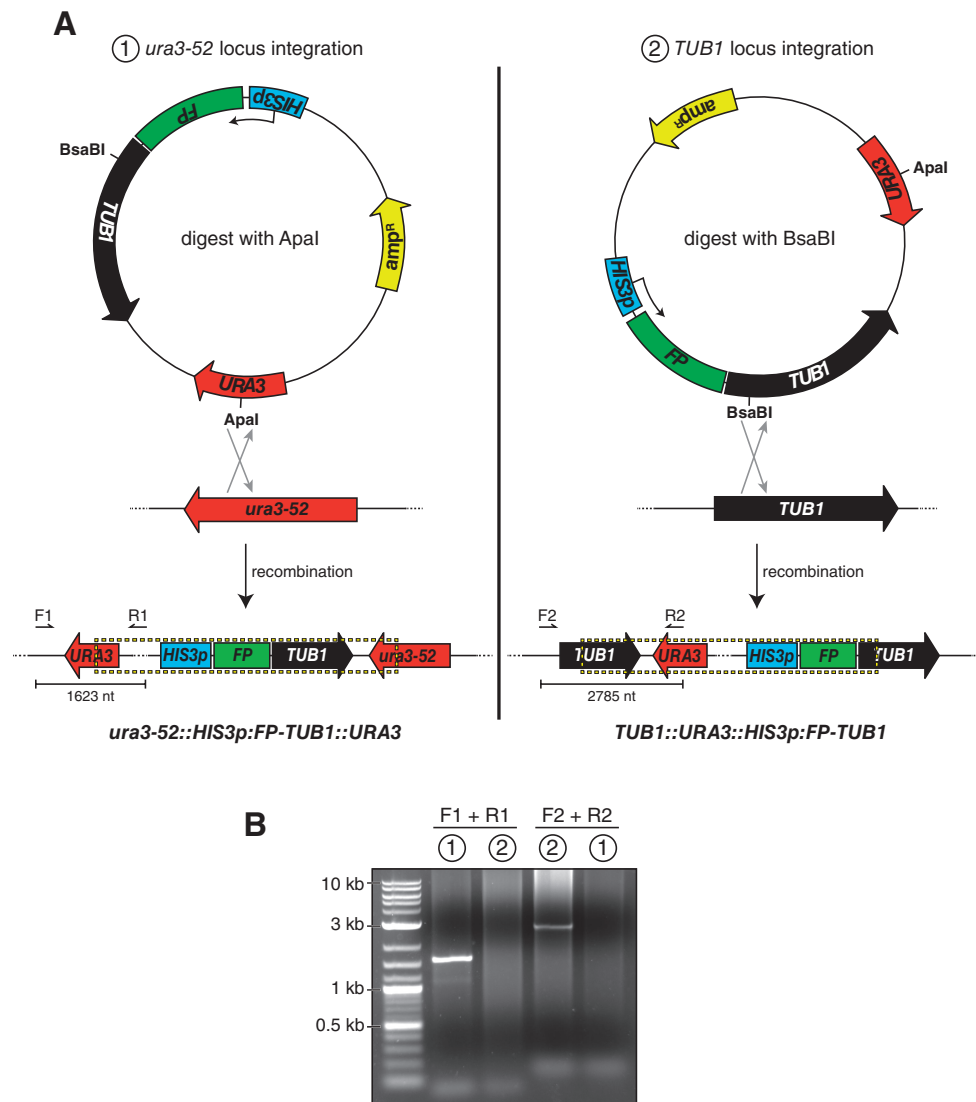


Figure 1: Differential FP-Tub1 integration strategies. A) Schematics depicting Tub1-tagging plasmid pRS306:*HIS3p:FP-TUB1* and chromosomal loci *ura3-52* and *TUB1*, with open reading frame and direction of coding sequence indicated (*HIS3p*, *HIS3* promoter; *FP*, fluorescent protein; *TUB1*, alpha-tubulin; *URA3*, auxotrophic marker; *amp^R*, beta-lactamase). Restriction digest by either *Apal* (left; cuts within *URA3* gene) or *BsaBI* (right; cuts within *TUB1* gene) targets the plasmid for homologous recombination into either the *ura3-52* or the *TUB1* locus as depicted. Dashed box below delineates chromosomally integrated plasmid. Arrows indicate the forward (i.e. F1 and F2) and reverse (i.e. R1 and R2) diagnostic PCR primers (see Table 1). B) Ethidium bromide-stained agarose gel with PCR products from genomic DNA isolated from yeast strains transformed with either (i) *Apal*-digested or (ii) *BsaBI*-digested pRS306:*HIS3p:mCherry-TUB1* using the indicated primers. Note the specificity of each PCR product, and thus the ability to target the plasmid for chromosomal integration into either the *ura3-52* or the *TUB1* locus by differential restriction digest.

Interestingly, we found that although the *ura3-52* locus-integrated *HIS3p:mCherry-TUB1* exhibited no synthetic genetic interaction with either *bik1Δ* or *bim1Δ*, the *TUB1* locus-integrated allele showed a strong synthetic interaction with both *bik1Δ* and *bim1Δ*

mutations (Table 2). These data indicate that the *TUB1* locus-integrated *mCherry-TUB1* construct, but not the *ura3-52* locus-integrated construct, interferes with microtubule function. This is surprising given that neither the upstream promoter region nor the open reading frame

Table 1: Primers used in this study

Primer	Purpose	Primer sequence
F1	To confirm <i>URA3</i> locus integration	5'-GGCCATGAAGCTTTTCTTTCC-3'
R1	To confirm <i>URA3</i> locus integration	5'-CAGGAAGGCAAAATGCCG-3'
F2	To confirm <i>TUB1</i> locus integration	5'-CACCCAAGATCTGTAACTTACAAC-3'
R2	To confirm <i>TUB1</i> locus integration	5'-GCGGGTGTATACAGAATAGC-3'

Table 2: Summary of genetic interactions

Locus	Tub1 fusion	<i>bik1Δ</i>	<i>bim1Δ</i>
<i>ura3-52</i>	mCherry	—	—
<i>TUB1</i>	mCherry	+++	+++
<i>ura3-52</i>	mTurquoise2	—	—
<i>TUB1</i>	mTurquoise2	+++	++
<i>ura3-52</i>	Venus	—	—
<i>TUB1</i>	Venus	++	++
<i>TUB1</i>	mRuby2	+++	++
<i>TUB1+3' UTR</i>	mRuby2	—	—
<i>TUB1+3' UTR</i>	Venus	+	n/t
<i>TUB1+3' UTR</i>	mTurquoise2	—	n/t
<i>TUB1+3' UTR</i>	mEos2	—	n/t
<i>TUB1+3' UTR</i>	yomWasabi	+	n/t

—, no synthetic interaction; + or ++, synthetic sick; +++, synthetic lethal; n/t, not tested.

of the endogenous *TUB1* locus was affected by the plasmid integration in both scenarios (see Figure 1A).

To determine whether the observed synthetic growth defects were due to the specific FP tag, we generated similar FP-Tub1 constructs in which mCherry was replaced by either mTurquoise2, Venus or mRuby2. These are improved (i.e. brighter and/or more photostable) variants of their respective predecessor FPs (i.e. CFP, YFP and mCherry) (22–24). Yeast strains with these new *FP-TUB1* constructs targeted to the *TUB1* locus also exhibited strong synthetic interactions with both *bik1Δ* and *bim1Δ* mutations; however, none of the *ura3-52* locus-targeted constructs tested showed synthetic defects with either *bik1Δ* or *bim1Δ* (Table 2). These results indicate that the synthetic interactions, and thus the defects in microtubule function, are not a consequence of fluorophore selection, but are in fact due to the choice of the site for plasmid integration.

Addition of *TUB1* 3' UTR to *FP-Tub1* constructs rescues microtubule dysfunction

Because only the *TUB1*-targeted, but not the *ura3-52*-targeted, *FP-Tub1* constructs were observed to negatively

affect microtubule function, we reasoned that a possible cause for this discrepancy was the disruption of the *TUB1* locus upon homologous recombination. Following integration into the *TUB1* locus, the native 3' untranslated region (3'UTR) becomes linked to the *FP-TUB1*, but not the untagged *TUB1* gene (see dashed box in Figure 1A, right). The 3'UTR sequence found in mRNA transcripts often regulates translational control (25). Thus, uncoupling of the endogenous *TUB1* gene from its 3'UTR might lead to altered Tub1 protein levels, which might consequently affect microtubule function.

We asked if restoring the 3'UTR to the endogenous, untagged *TUB1* gene would rescue the synthetic defects with *bim1Δ* or *bik1Δ* mutations. To this end, we altered the *FP-Tub1*-tagging plasmids by adding an additional 618 nucleotides corresponding to the region downstream of the *TUB1* locus (Figure 2A). This sequence was chosen because it extends well beyond the last potential polyadenylation sequence (AATAAA, 145 nt downstream of the stop codon; ATTAAA, 540 nt downstream of the stop codon). Following transformation with the new *BsaBI*-digested plasmid (*pHIS3p:FP-TUB1+3'UTR*), both the endogenous, untagged *TUB1* and the *FP-TUB1* genes will be immediately followed by the 3'UTR sequence (Figure 2A, dashed box). Strikingly, we found that most of the *FP-TUB1+3'UTR* constructs tested exhibited no synthetic genetic interactions with *bik1Δ* (Tables 2 and 3; Figure 2B, compare growth of colonies boxed in red), indicating that the observed defects in microtubule function were a consequence of disruption of the *TUB1* 3'UTR sequence. Notably, two of seven *Venus-TUB1+3'UTR* isolates and one of six *yomWasabi-TUB1+3'UTR* isolates exhibited a synthetic interaction when crossed with *bik1Δ*, producing tetrad progeny that could sometimes form microcolony (Table 3). In cases that we tested, analytical PCR suggested that the plasmid integrated as expected (data not shown). Although the reason for the isolate-dependent

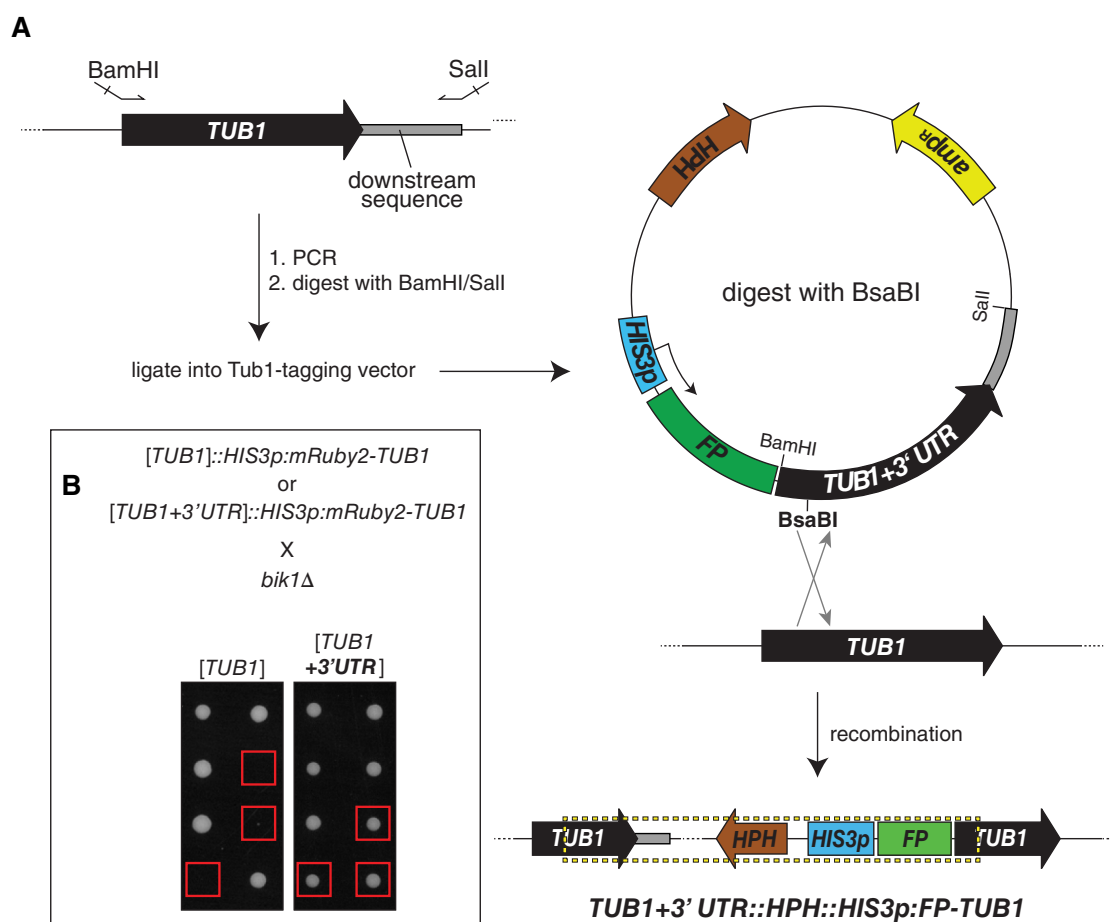


Figure 2: Addition of 3'UTR to integration plasmid rescues synthetic lethality with *bik1Δ*. A) Schematic depicting strategy for construction of *TUB1*+3' UTR-integration plasmids. Arrows indicate forward and reverse primers used for PCR, which include BamHI and Sall restriction sites for cloning. Restriction digest by BsaBI targets the plasmid for homologous integration into the *TUB1* locus, as depicted. Dashed box delineates chromosomally integrated plasmid. B) Representative tetrad progeny of indicated crosses. Red boxes indicate *bik1Δ* *TUB1*::*HIS3p::mRuby2-TUB1* progeny and *bik1Δ* *TUB1*+3' UTR::*HIS3p::mRuby2-TUB1* progeny as assessed by marker analysis.

Table 3: Viability of strains with indicated *TUB1*+3' UTR::*HIS3p::FP-TUB1*-integrated vectors in combination with *bik1Δ* mutant

FP- <i>TUB1</i> strains crossed with <i>bik1Δ</i> ^a	Number of tetrads analyzed	Number of double mutants	Viability of double mutants	
			Viable	Microcolony
Venus- <i>TUB1</i>	60	75	59	16
mEos2- <i>TUB1</i>	51	53	53	0
mRuby2- <i>TUB1</i>	27	31	31	0
yomWasabi- <i>TUB1</i>	49	62	56	6
mTurquoise2- <i>TUB1</i>	35	41	41	0

^aAt least four independent isolates were analyzed for synthetic defects. Number indicates the combined total of tetrads or progeny from all isolates. Two of seven Venus-*TUB1* isolates and one of six yomWasabi-*TUB1* isolates showed synthetic growth defects when combined with *bik1Δ*, producing tetrad progeny that could sometimes form microcolony.

differences is unknown, we noted that Venus- and yomWasabi-Tub1+3'UTR isolates that exhibited synthetic growth defects with *bik1Δ* displayed higher FP-Tub1 fluorescence intensity when compared with isolates that did not exhibit synthetic interaction (Figure S1, Supporting Information for Venus-Tub1+3'UTR; data not shown for yomWasabi-Tub1+3'UTR). Thus, defects in microtubule function observed in both cases could be due to a higher expression level of FP-Tub1. These results indicate the importance of confirming functionality of a chromosomally integrated Tub1-tagging plasmid, and also indicate the usefulness of the synthetic genetic analysis for such a test.

Comparative analysis of different FP-Tub1+3' UTR-tagging vectors

We next sought to compare the brightness and photostability of the different *TUB1*-locus-targeted FP-Tub1 constructs. Figure 3A shows representative fluorescence images of cells expressing mTurquoise2-Tub1, yomWasabi-Tub1, Venus-Tub1, mRuby2-Tub1 and mEos2-Tub1 (pre- and post-photoconversion), all acquired using identical imaging conditions (see *Materials and Methods*). mEos2 is a photoconvertible FP that exhibits green FP-like properties ($\lambda_{\text{ex}} = 506 \text{ nm}$; $\lambda_{\text{em}} = 519 \text{ nm}$) until exposed to 405-nm light, after which it switches irreversibly to exhibiting red FP-like properties ($\lambda_{\text{ex}} = 573 \text{ nm}$; $\lambda_{\text{em}} = 584 \text{ nm}$) (26). In addition, we also generated a plasmid with which to tag Tub1 with Clover GFP. Although we managed to confirm integration of the *Clover-TUB1+3'UTR* plasmid by fluorescence microscopy, the low intensity of this FP makes it a poor choice for live cell imaging. However, given its spectral properties, this construct could conceivably be a good choice for fluorescence resonance energy transfer (FRET) studies (23).

To compare the relative brightness between the different fluorophores, we synchronized FP-Tub1-expressing cells in S phase using hydroxyurea (HU) and measured the fluorescence intensity of the entire preanaphase spindle. Synchronization allowed us to avoid differences in fluorescence intensities arising from differences in spindle assembly state. To determine the relative photostability of each FP-Tub1 construct, we measured the fluorescence intensity of a given spindle over time, and then plotted and fit the values to a single exponential. As quantified in Figure 3C,D, mTurquoise2-, Venus- and mRuby2-Tub1

were the brightest, while mTurquoise2-, Venus- and post-converted mEos2-Tub1 were the most photostable (also see images in Figure 3B for the analysis in Figure 3D). Irrespective of differences in brightness or photostability, even the dimmest, most non-photostable of the FP-Tub1 constructs shown in Figure 3 (i.e. yomWasabi and mEos2) were suitable for time-lapse fluorescence microscopy experiments. The various FP-Tub1 constructs span the spectrum of FPs, and offer useful tools for multicolor fluorescence microscopy imaging studies.

mEos2-Tub1 enables photo-marking of spindle microtubules in living yeast cells

We found that mEos2-Tub1 could be efficiently photoconverted from green to red using both wide-field fluorescence (Figure 4A) and laser scanning confocal microscopy (Figure 4B). Unlike photoactivatable FPs (e.g. PA-GFP and PA-mCherry), which are dark until turned on by a pulse of 405-nm light, photoconvertible FPs offer the advantage of being observable prior to conversion. The preactivated dark state of the PA-FPs complicates identification of the cellular structure of interest (e.g. the spindle) and thus the appropriate targeting of the 405 nm pulse of light.

To test the utility of mEos2-Tub1, we performed localized photoconversion and monitored green (preconverted) and red (postconverted) fluorescence over time. Using confocal microscopy, we targeted half of a preanaphase spindle (Figure 4B) or the midzone area of an anaphase spindle (Figure 4C) for photoconversion. As shown in Figure 4B,C, upon localized 405-nm illumination, we observed strong photoconversion of green to red fluorescence. However, because of the short duration of our imaging conditions, we did not observe significant tubulin turnover, as expected from previous laser-photobleaching studies (19,27). While these results only demonstrate the effectiveness of the photoconversion, they suggest that mEos2-Tub1 will prove beneficial for monitoring tubulin turnover in future studies.

Comparative analysis of FP-Tub1+3'UTR with older FP-Tub1 fusions

To test whether the new *FP-TUB1+3'UTR*-tagging vectors would constitute better reagents than those currently used in the field (e.g. *CFP-TUB1*, *mCherry-TUB1* and *GFP-TUB1*), we performed side-by-side comparisons

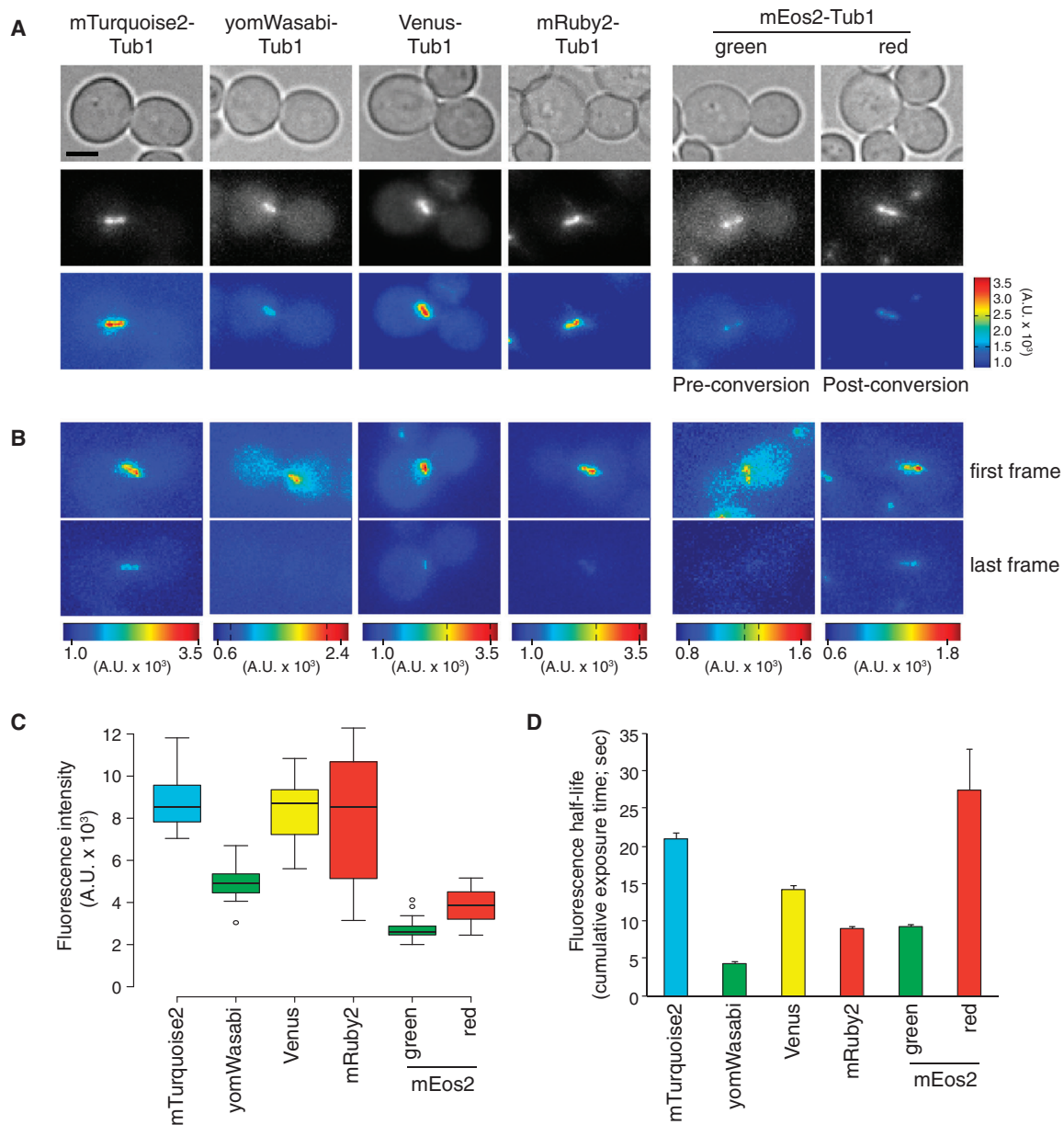


Figure 3: Fluorescence intensities and half-lives of FP-Tub1 constructs. A) Representative images depicting HU-arrested FP-Tub1-expressing cells (transformed by *TUB1*+3' UTR plasmids). To depict relative fluorescence intensities, all color map images are shown with the same brightness and contrast settings (see color bar on the right for intensity scale). B) Representative fluorescence images illustrating fluorescence half-life of each FP-Tub1 construct. Time-lapse images of FP-Tub1 were acquired every 5 seconds for 10 min. Color maps of first ($t=0$ second) and last ($t=600$ seconds) frame are shown. For (A) and (B), each image is a maximum-intensity projection of a 3- μ m Z stack (0.5- μ m step size) of wide-field images. Scale bar, 3 μ m. C) Box plot of fluorescence intensity values measured for HU-arrested spindles (see *Materials and Methods*; $n=20$ spindles). Whiskers define the range, boxes encompass 25th to 75th quartiles, lines depict the medians and circles depict outlier values [defined as values greater than (upper quartile + $1.5 \times$ interquartile distance) or less than (lower quartile - $1.5 \times$ interquartile distance)]. D) Plot depicting fluorescence half-life of each FP-Tub1 construct. Intensity measurements for HU-arrested spindles ($n=5$ spindles) over time were plotted and fit to a single exponential. Values take into account cumulative exposure time. All measurements for post-photoconverted (red) mEos2 were acquired after a 5-second pulse of 405-nm light (see *Materials and Methods*).

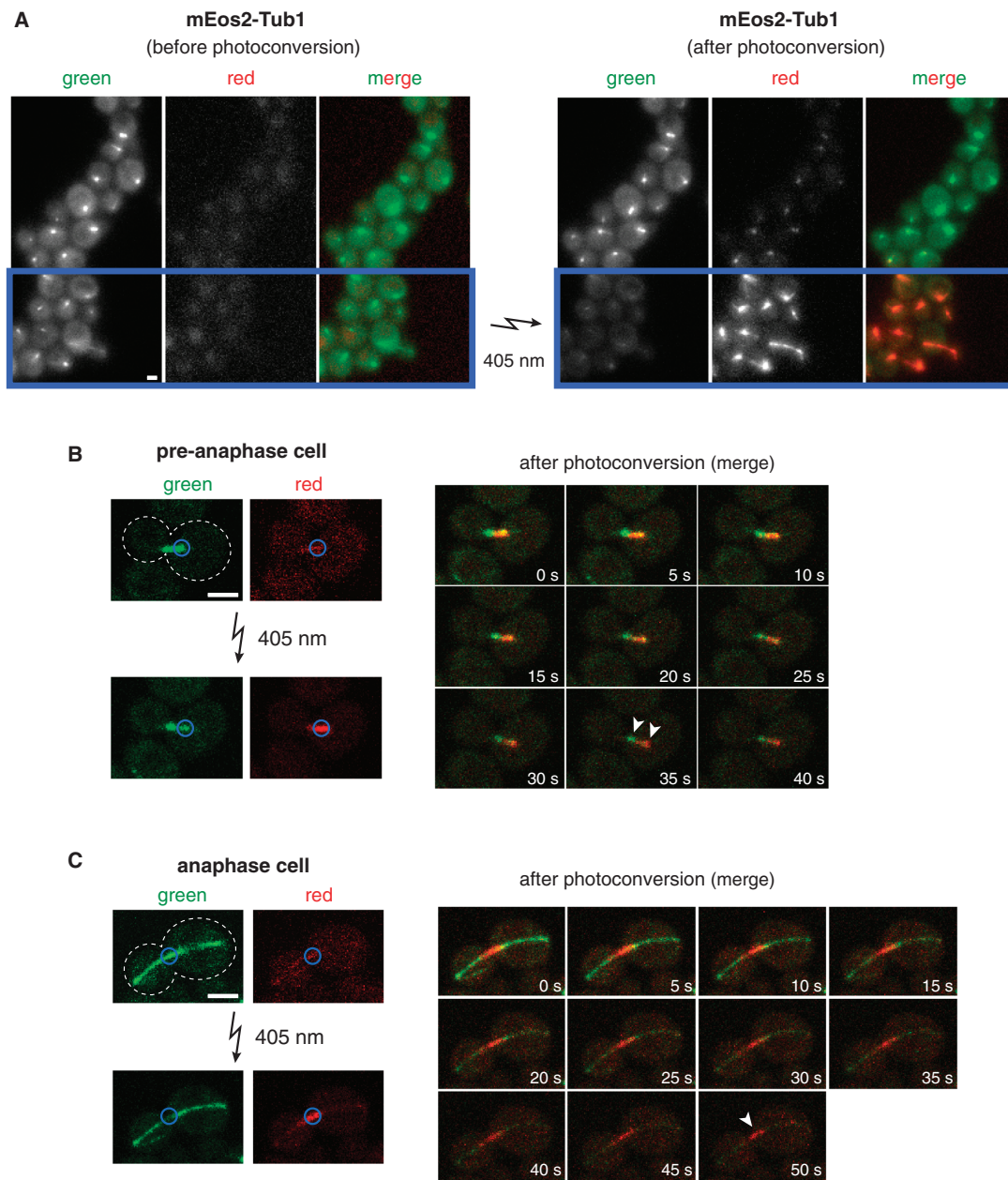


Figure 4: Photoconversion of mEos2-Tub1 using wide-field and confocal fluorescence microscopy. A) Representative image depicting mEos2-Tub1-expressing cells before (left) and after (right) photoconversion. Blue box indicates area in the field targeted for exposure to 5-second pulse of 405-nm light (by reducing field diaphragm). Note the reduction in green fluorescence concomitant with the appearance of red fluorescence following photoconversion. Scale bar, 2 μ m. B) Example of a mEos2-Tub1-expressing preanaphase cell subjected to local photoconversion by laser scanning confocal fluorescence microscopy. Half of the preanaphase spindle (marked by blue circle) was exposed to a brief 405-nm laser pulse. Pre- (green) and post- (red) photoconverted mEos2-Tub1 fluorescence were subsequently imaged every 5 seconds for 40 seconds. Clear separation of green and red fluorescence at $t = 35$ seconds (arrowheads) indicates low turnover of tubulin within the spindle in this timeframe. Scale bar, 3 μ m. C) Similar to (B) but the spindle midzone of an anaphase cell was photoconverted. Green and red fluorescence were subsequently imaged every 5 seconds for 50 seconds. White arrowhead indicates persistence of photoconverted mark at $t = 50$ seconds, suggesting low turnover of interpolar spindle microtubules within the indicated timeframe. Scale bar, 3 μ m.

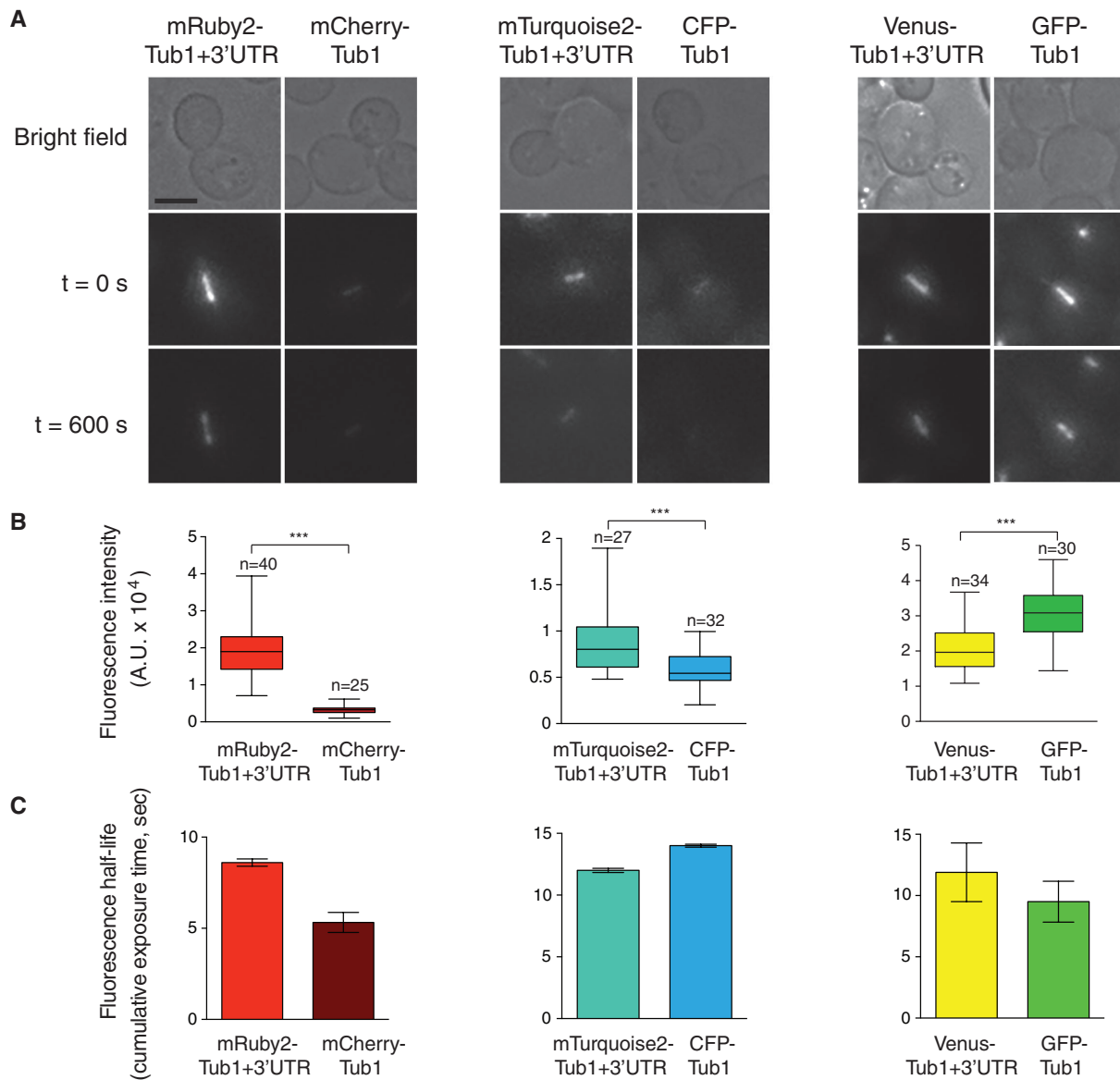


Figure 5: Side-by-side comparison of *TUB1*+3'UTR-FP with older FP-*TUB1* constructs. A) HU-arrested cells expressing indicated FP-Tub1 were imaged for 10 min with 10-second intervals. First ($t = 0$ second) and last ($t = 600$ seconds) frame are shown. Each fluorescence image is a maximum intensity projection of a 3- μ m Z stack with 0.5- μ m step size. Scale bar, 3 μ m. B) Box plot of fluorescence intensity values measured for preanaphase spindles. Whiskers define the range, boxes encompass 25th to 75th quartile and lines indicate the median. *** $p \leq 0.0001$ by Student's t -test. C) Plot of fluorescence half-life of each FP-Tub1 construct. Time-lapse images were acquired continuously for 5 min. Next, intensity measurements for preanaphase spindles ($n = 5$ spindles) over time were plotted and fitted to a single exponential. Values take into account cumulative exposure time. Error bars represent 95% confidence intervals.

of brightness, photostability and visibility of astral microtubules, using identical imaging conditions (see *Materials and Methods*). We found that mRuby2-Tub1+3'UTR and mTurquoise2-Tub1+3'UTR were significantly

brighter than mCherry-Tub1 and CFP-Tub1, respectively (Figure 5A,B). The photostability of mRuby2-Tub1+3'UTR was significantly higher than mCherry-Tub1, whereas that of mTurquoise2-Tub1+3'UTR was

comparable to CFP-Tub1 (Figure 5C). Additionally, we observed that Venus-Tub1+3'UTR was dimmer but more photostable when compared with GFP-Tub1. Furthermore, cells expressing mRuby2-Tub1+3'UTR and mTurquoise2-Tub1+3'UTR displayed brighter astral microtubules (Figure 6A and data not shown) and a higher frequency of finding astral microtubules (Figure 6B) when compared with mCherry-Tub1 and CFP-Tub1, respectively. Cells expressing Venus-Tub1+3'UTR and GFP-Tub1 exhibited similar visibility of astral microtubules (Figure 6B). Because astral microtubules are few (16) and are usually difficult to image, these results suggest that the new *FP-TUB1*+3'UTR-tagging vectors are improved plasmids for FP tagging of microtubules in budding yeast.

Availability of a new set of FP-Tub1-tagging plasmids

To broaden the flexibility and utility of the *FP-TUB1*+3'UTR cassettes, we substituted the hygromycin resistance marker in each plasmid with four different selectable markers: *URA3*, *LEU2*, *TRP1* and *HIS3* (Figure 7). With the exception of the *HIS3*-containing plasmids, which require digestion with *Xba*I, *Bsa*BI linearizes each and targets them for integration into the *TUB1* locus (see Table 4). All plasmids listed in Table 4 have been deposited at Addgene (<http://www.addgene.com>) for distribution to academic researchers.

Materials and Methods

Media and strain construction

All strains were derived from YWL36 or YWL37 (28) and are available upon request. We transformed yeast strains using the lithium acetate method (29). Transformants were clonally purified by streaking to individual colonies on selective media. Insertion of tagging cassette was confirmed either by PCR (see Figure 1B) or by fluorescence microscopy. Yeast synthetic defined (SD) media were obtained from Sunrise Science Products.

Construction of FP-Tub1-tagging vectors

To generate vectors for integration of a *HIS3p*-driven *FP-TUB1::URA3* cassette into the *ura3-52* locus, *Venus*, *mTurquoise2* or *mRuby2* were PCR amplified from pFA6a-link-*yEVENUS*-KAN (2), *pmTurquoise2-tubulin* (Addgene) (22) or *pcDNA3:mRuby2* (Addgene) (23), respectively. The forward and reverse PCR primers included a 20-nucleotide 5' extension that was complementary to regions flanking the *mCherry* coding sequence (forward:

5'-AAGATAACGAAGGCAAAGC-3'; reverse: 5'-AATAACTTCTC TCATGGATC-3') in pAK011 (also known as pRS306:*HIS3p::mCherry-TUB1*) (15). After digesting pAK011 with *Bam*HI and *Xho*I (to excise *mCherry*), the PCR products were assembled with the gel purified vector via Gibson assembly reaction (30). Briefly, a 5 μ L mixture of PCR product and vector was combined with a 15 μ L mixture of T5 exonuclease (Epicentre), Phusion high-fidelity DNA polymerase (New England Biolabs) and Taq DNA ligase (New England Biolabs), and incubated at 50°C for 15 min. Proper assembly was verified by restriction digest and DNA sequencing, yielding pRS306:*HIS3p::Venus-TUB1*, pRS306:*HIS3p::mTurquoise2-TUB1* and pRS306:*HIS3p::mRuby2-TUB1* (see Figure 1).

To generate a vector for integration of *HIS3p::mCherry-TUB1::HPH* (hygromycin resistance cassette) into the *TUB1* locus, the *HIS3p::mCherry-TUB1* cassette was amplified from pAK011 and ligated into *Xma*I- and *Sal*I-digested pAG32 (31) using the Gibson assembly reaction, as above, yielding p*HIS3p::mCherry-TUB1::HPH*. Subsequently, *Venus*, *mTurquoise2* and *mRuby2* were amplified as above and assembled into *Xho*I- and *Bam*HI-digested p*HIS3p::mCherry-TUB1::HPH* vector via Gibson assembly reaction, yielding p*HIS3p::Venus-TUB1::HPH*, p*HIS3p::mTurquoise2-TUB1::HPH* and p*HIS3p::mRuby2-TUB1::HPH*. Clover, *yomWasabi* (improved GFP; Allele Biotechnology) and *mEos2* were amplified from pcDNA3:*Clover* (Addgene) (23), pFA6a-link-*yomWasabi*-KAN (Addgene) (1) and pRSETa:*mEos2* (Addgene) (26), respectively, using primers flanked with *Xho*I (forward) and *Bam*HI (reverse) restriction sites. The PCR products were digested with *Xho*I and *Bam*HI, and ligated into p*HIS3p::mCherry-TUB1::HPH* digested similarly, yielding p*HIS3p::Clover-TUB1::HPH*, p*HIS3p::yomWasabi-TUB1::HPH* and p*HIS3p::mEos2-TUB1::HPH*.

To generate vectors for integration into the *TUB1* locus without disrupting the putative *TUB1* 3'UTR sequence (see Figure 2), we amplified the entire *TUB1* open reading frame (including the 116-nucleotide intron) plus 618 nucleotides of downstream genomic sequence following the stop codon using PCR primers flanked with *Bam*HI (forward) and *Sal*I (reverse) sites. The PCR product was digested with *Bam*HI and *Sal*I, and ligated into each respective vector (i.e. p*HIS3p::FP-TUB1::HPH*) digested similarly (to excise *TUB1*), yielding p*HIS3p::FP-TUB1+3'UTR::HPH* (see Figure 2 and Table 4).

Next, to generate vectors with different selectable markers, we amplified respective markers from pRS303 (*HIS3*), pRS304 (*TRP1*), pRS305 (*LEU2*) and pRS306 (*URA3*) using PCR primers flanked with *Asc*I (forward) and *Spe*I (reverse) sites. The PCR products were digested with *Asc*I and *Spe*I, and ligated into p*HIS3p::FP-TUB1::HPH* digested similarly, yielding p*HIS3p::FP-TUB1+3'UTR::MARKER* (see Figure 7 and Table 4 for a listing of all plasmids).

Construction of FP-Tub1-expressing strains

To integrate the FP-Tub1-tagging vectors into the *ura3-52* or *TUB1* locus, we transformed yeast strains with *Apal*I-linearized (pRS306 vectors; for integration into *ura3-52* locus), *Bsa*BI-linearized (all

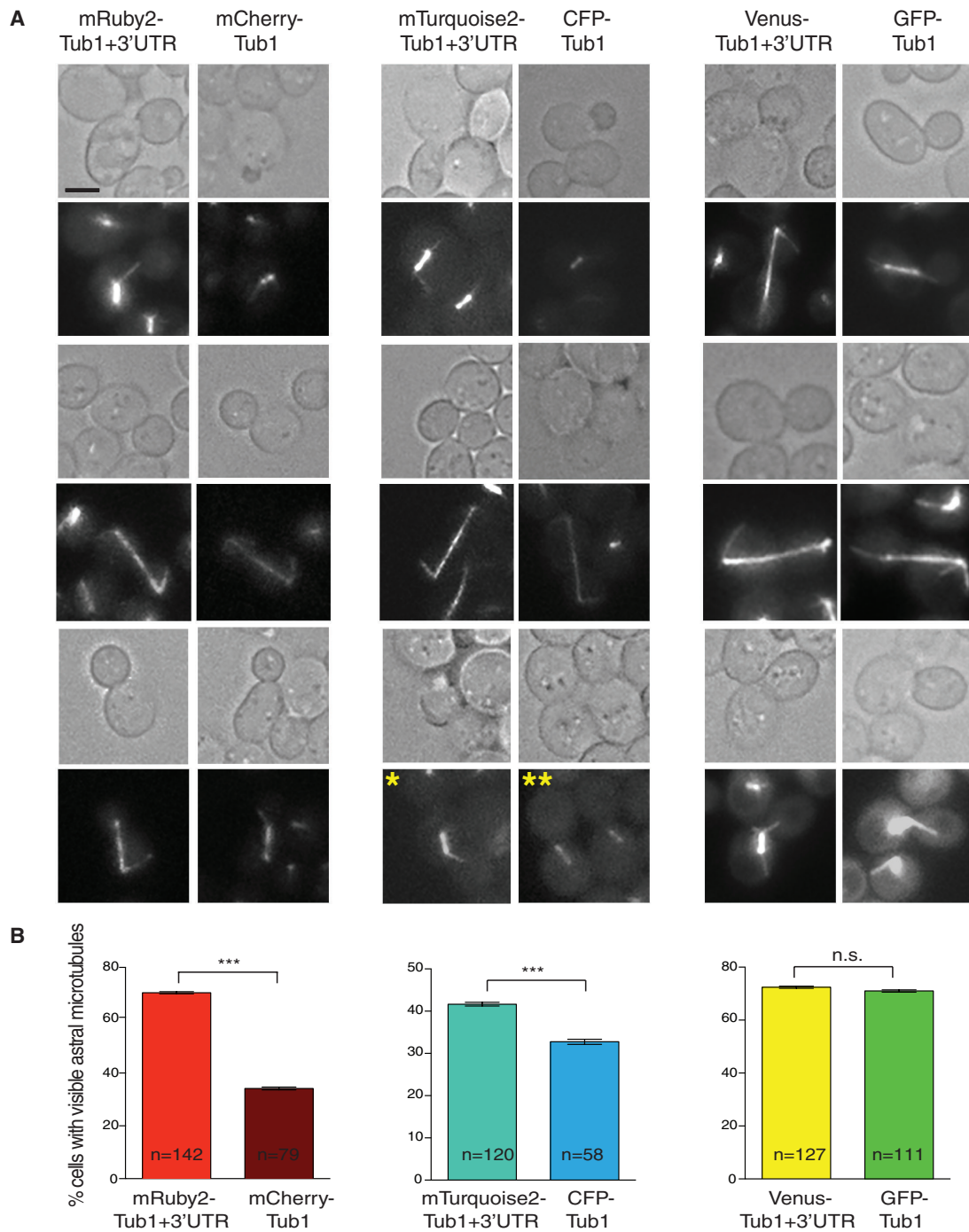


Figure 6: Side-by-side comparison of astral microtubules visualized by *TUB1*+3' UTR-FP with older FP-*TUB1* constructs. A) Representative fluorescence images of astral microtubules of each FP-Tub1 fusions. Each image is a maximum intensity projection of a 1- μ m Z stack with 0.5- μ m step size, with 2 \times averaging of 80-millisecond exposure for each frame. Note that the exposure to capture clear astral microtubules was higher than that needed for mitotic spindle as in Figures 3 and 5. Asterisk (*) indicates an example of a cell with visible astral microtubule [for scoring in (B)], whereas double asterisk (**) indicates an example of cells with no visible astral microtubules. Scale bar, 3 μ m. B) Frequency of observing astral microtubules for each indicated FP-Tub1. Error bar represents standard error of proportion. *** $p < 0.0001$, and n.s., not significant, by Student's *t*-test.

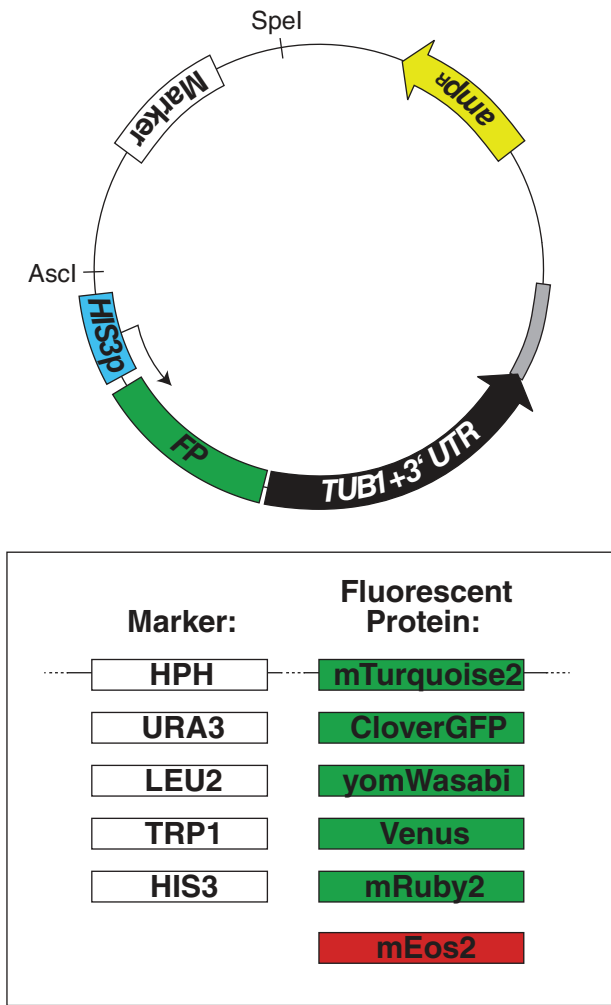


Figure 7: Overview of the plasmids generated for fluorescent labeling of microtubules. General map of the plasmids generated in this study. Also see Table 4.

pHIS3p:FP-TUB1::MARKER and *pHIS3p:FP-TUB1+3' UTR::MARKER* plasmids, except for *pHIS3p:FP-TUB1+3' UTR::HIS3*; for integration into *TUB1* locus) or *XbaI*-linearized (*pHIS3p:FP-TUB1+3' UTR::HIS3* vectors; for integration into *TUB1* locus) plasmids. To label microtubules using previously published plasmids, wild-type strains were transformed with *StuI*-digested *pAK011* (*mCherry-TUB1::URA3*) (14,32) or *StuI*-digested *pAFS125C* (*CFP-TUB1::URA3*) (18,33–35), or undigested *pBJ1351* (*GFP-TUB1::LEU2*) (12,36–39). Hygromycin-resistant *His*⁺, *Trp*⁺, *Leu*⁺ or *Ura*⁺ transformants were selected and examined for FP-Tub1 fluorescence by microscopy.

Image acquisition and photoconversion

To acquire images of preanaphase spindles for fluorescence intensity and half-life measurements (Figures 3 and 5), cells were grown to early log phase in SD media and then arrested in S phase by adding

Table 4: Tub1-tagging plasmids for integration into *TUB1* locus

Plasmid	Selectable marker	Digest for integration
pHIS3p:mTurquoise2-Tub1+3'UTR::HPH	HPH	BsaBI
pHIS3p:CloverGFP-Tub1+3'UTR::HPH	HPH	BsaBI
pHIS3p:yomWasabi-Tub1+3'UTR::HPH	HPH	BsaBI
pHIS3p:Venus-Tub1+3'UTR::HPH	HPH	BsaBI
pHIS3p:mRuby2-Tub1+3'UTR::HPH	HPH	BsaBI
pHIS3p:mEos2-Tub1+3'UTR::HPH	HPH	BsaBI
pHIS3p:mTurquoise2-Tub1+3'UTR::URA3	URA3	BsaBI
pHIS3p:CloverGFP-Tub1+3'UTR::URA3	URA3	BsaBI
pHIS3p:yomWasabi-Tub1+3'UTR::URA3	URA3	BsaBI
pHIS3p:Venus-Tub1+3'UTR::URA3	URA3	BsaBI
pHIS3p:mRuby2-Tub1+3'UTR::URA3	URA3	BsaBI
pHIS3p:mEos2-Tub1+3'UTR::URA3	URA3	BsaBI
pHIS3p:mTurquoise2-Tub1+3'UTR::LEU2	LEU2	BsaBI
pHIS3p:CloverGFP-Tub1+3'UTR::LEU2	LEU2	BsaBI
pHIS3p:yomWasabi-Tub1+3'UTR::LEU2	LEU2	BsaBI
pHIS3p:Venus-Tub1+3'UTR::LEU2	LEU2	BsaBI
pHIS3p:mRuby2-Tub1+3'UTR::LEU2	LEU2	BsaBI
pHIS3p:mEos2-Tub1+3'UTR::LEU2	LEU2	BsaBI
pHIS3p:mTurquoise2-Tub1+3'UTR::TRP1	TRP1	BsaBI
pHIS3p:CloverGFP-Tub1+3'UTR::TRP1	TRP1	BsaBI
pHIS3p:yomWasabi-Tub1+3'UTR::TRP1	TRP1	BsaBI
pHIS3p:Venus-Tub1+3'UTR::TRP1	TRP1	BsaBI
pHIS3p:mRuby2-Tub1+3'UTR::TRP1	TRP1	BsaBI
pHIS3p:mEos2-Tub1+3'UTR::TRP1	TRP1	BsaBI
pHIS3p:mTurquoise2-Tub1+3'UTR::HIS3	HIS3	XbaI
pHIS3p:CloverGFP-Tub1+3'UTR::HIS3	HIS3	XbaI
pHIS3p:yomWasabi-Tub1+3'UTR::HIS3	HIS3	XbaI
pHIS3p:Venus-Tub1+3'UTR::HIS3	HIS3	XbaI
pHIS3p:mRuby2-Tub1+3'UTR::HIS3	HIS3	XbaI
pHIS3p:mEos2-Tub1+3'UTR::HIS3	HIS3	XbaI

200 mM HU. After 2.5 h in HU-containing media, cells were mounted on a 1.5% agarose pad containing non-fluorescent SD media supplemented with HU. Wide-field fluorescence images were collected as previously described (40) using a 1.45 NA 100× objective on a Nikon 80i upright microscope equipped with piezo Z control (Physik Instrumente), electronically controlled SmartShutter (Sutter Instrument), motorized filter cube turret and a cooled EM-CCD Cascade-II camera (Photometrics). The microscope system was controlled by NIS-Elements software (Nikon). Sputtered/ET filter cube sets (Chroma Technology) were used for imaging mTurquoise2 or CFP (49001), yomWasabi or GFP or preconverted mEos2 (49002), Venus (49003) and mRuby2 or mCherry or postconverted mEos2 (49008) fluorescence. Z-stack images of 2 or 3 μm thick were acquired with a step size of 0.5 μm. Images of FP-Tub1 were acquired every 5 seconds for 10 min (Figure 3) or every 10 seconds for 10 min (Figure 5A) or with no interval for 5 min (Figure 5C). For Figure 3, all images were acquired using 30-millisecond exposure. For photostability measurements (Figures 3 and 5C), we used ImageJ (NIH) to draw a box outlining the HU-arrested spindle to quantify the fluorescence intensity of each spindle. An adjacent, non-overlapping region within the same cell was used for background subtraction. The decay

in fluorescence intensity was fitted by Matlab or Kaleidagraph using the equation $y = a * e^{(-b * x)}$. The half-life was calculated as $0.693/b$. For comparison of the intensity of FP-Tub1+3'UTR with older FP-Tub1 fusions, identical exposure was used for each pair (60 milliseconds for Tub1+3'UTR-mRuby2 versus Tub1-mCherry; 50 milliseconds for Tub1+3'UTR-mTurquoise2 versus Tub1-CFP; 35 milliseconds for Tub1+3'UTR-Venus and Tub1-GFP). For comparing the frequency of observing astral microtubules between the new FP-Tub1+3'UTR and the older FP-Tub1 fusions (see Figure 6A for examples of cells showing visible astral microtubules), we acquired Z-stack images of 2 μ m thickness with 0.5 μ m step size and 2 \times averaging of 80-millisecond exposure. All images used for comparison were acquired on the same day to ensure that any changes to the mercury arc lamp bulb were negligible.

To photoconvert mEos2 (from green to red) using wide-field fluorescence microscopy (Figure 4A), cells were exposed to a pulse of 405-nm light for 5 seconds using the mercury arc lamp and a D405/20 filter cube (Chroma Technology). Local photoconversion was achieved by closing down the field diaphragm, thus restricting the area of excitation. Images of green and red fluorescence were acquired before and after the 405-nm light exposure using the same camera settings (see Figure 4A). To photoconvert a half-spindle (Figure 4B), we used a 1.45 NA 100 \times objective on a Nikon A1-R confocal microscope (Marine Biological Laboratory) equipped with 405-, 488- and 561-nm laser lines. Spindles were locally photoconverted for 1–2 seconds using an attenuated 405-nm laser power (at 0.4%) followed by two-color time-lapse acquisition of three optical sections (0.5- μ m step size) with 488- and 561-nm lasers.

Acknowledgments

This work was supported by an American Heart Association Undergraduate Summer Fellowship to K. B. and an NIH/NIGMS grant (1R01GM076094) to W. L. L. The work was also supported in part by a competitive research award to W. L. L. from the Robert Day Allen Fellowship Fund, the Erik B. Fries Endowed Fellowship Fund and the Laura and Arthur Colwin Endowed Summer Research Fellowship Fund of the Marine Biological Laboratory in Woods Hole, MA, where a portion of this work was conducted under the auspices of this award. The authors declare that they have no conflict of interest.

Supporting Information

Additional Supporting Information may be found in the online version of this article:

Figure S1: Different colony isolates exhibit differential synthetic interactions with *bik1* Δ . A) Tetrad dissection progeny from a cross between *bik1* Δ and two independent isolates of *TUB1*+3'UTR::*HIS3p*::*Venus-TUB1*. Red boxes indicate *bik1* Δ haploid progeny expressing Venus-Tub1 (with genotype *TUB1*+3'UTR::*HIS3p*::*Venus-TUB1 bik1* Δ). B) Representative images illustrating differences in the fluorescence intensity values between the two isolates of *TUB1*+3'UTR::*HIS3p*::*Venus-TUB1* used in (A) for mating with *bik1* Δ . Each image was

acquired using identical acquisition settings (60-millisecond exposure; 4095 gain multiplier on the EM-CCD Cascade-II camera). Color maps are shown with the same brightness and contrast settings (see color bar for intensity scale). Each image is a maximum intensity projection of a 3- μ m Z stack (0.5 μ m step size) of wide-field images. Scale bar, 3 μ m.

References

- Lee S, Lim WA, Thorn KS. Improved blue, green, and red fluorescent protein tagging vectors for *S. cerevisiae*. *PLoS One* 2013;8:e67902.
- Sheff MA, Thorn KS. Optimized cassettes for fluorescent protein tagging in *Saccharomyces cerevisiae*. *Yeast* 2004;21:661–670.
- Longtine MS, McKenzie A III, Demarini DJ, Shah NG, Wach A, Brachat A, Philippsen P, Pringle JR. Additional modules for versatile and economical PCR-based gene deletion and modification in *Saccharomyces cerevisiae*. *Yeast* 1998;14:953–961.
- Young CL, Raden DL, Caplan JL, Czymmek KJ, Robinson AS. Cassette series designed for live-cell imaging of proteins and high-resolution techniques in yeast. *Yeast* 2012;29:119–136.
- Kaksonen M, Sun Y, Drubin DG. A pathway for association of receptors, adaptors, and actin during endocytic internalization. *Cell* 2003;115:475–487.
- Wloka C, Vallen EA, The L, Fang X, Oh Y, Bi E. Immobile myosin-II plays a scaffolding role during cytokinesis in budding yeast. *J Cell Biol* 2013;200:271–286.
- Woodruff JB, Drubin DG, Barnes G. Mitotic spindle disassembly occurs via distinct subprocesses driven by the anaphase-promoting complex, Aurora B kinase, and kinesin-8. *J Cell Biol* 2010;191:795–808.
- Carminati JL, Stearns T. Microtubules orient the mitotic spindle in yeast through dynein-dependent interactions with the cell cortex. *J Cell Biol* 1997;138:629–641.
- Straight AF, Marshall WF, Sedat JW, Murray AW. Mitosis in living budding yeast: anaphase A but no metaphase plate. *Science* 1997;277:574–578.
- Doyle T, Botstein D. Movement of yeast cortical actin cytoskeleton visualized *in vivo*. *Proc Natl Acad Sci USA* 1996;93:3886–3891.
- Luchniak A, Fukuda Y, Gupta ML Jr. Structure-function analysis of yeast tubulin. *Methods Cell Biol* 2013;115:355–374.
- Maddox P, Chin E, Mallavarapu A, Yeh E, Salmon ED, Bloom K. Microtubule dynamics from mating through the first zygotic division in the budding yeast *Saccharomyces cerevisiae*. *J Cell Biol* 1999;144:977–987.
- Jensen S, Segal M, Clarke DJ, Reed SI. A novel role of the budding yeast separin Esp1 in anaphase spindle elongation: evidence that proper spindle association of Esp1 is regulated by Pds1. *J Cell Biol* 2001;152:27–40.
- Khmelinskii A, Roostalu J, Roque H, Antony C, Schiebel E. Phosphorylation-dependent protein interactions at the spindle midzone mediate cell cycle regulation of spindle elongation. *Dev Cell* 2009;17:244–256.
- Khmelinskii A, Lawrence C, Roostalu J, Schiebel E. Cdc14-regulated midzone assembly controls anaphase B. *J Cell Biol* 2007;177:981–993.

16. Gupta ML Jr, Bode CJ, Thrower DA, Pearson CG, Suprenant KA, Bloom KS, Himes RH. β -Tubulin C354 mutations that severely decrease microtubule dynamics do not prevent nuclear migration in yeast. *Mol Biol Cell* 2002;13:2919–2932.
17. Fukuda Y, Luchniak A, Murphy ER, Gupta ML Jr. Spatial control of microtubule length and lifetime by opposing stabilizing and destabilizing functions of kinesin-8. *Curr Biol* 2014;24:1826–1835.
18. Markus SM, Plevock KM, St Germain BJ, Punch JJ, Meaden CW, Lee WL. Quantitative analysis of Pac1/LIS1-mediated dynein targeting: Implications for regulation of dynein activity in budding yeast. *Cytoskeleton (Hoboken)* 2011;68:157–174.
19. Kosco KA, Pearson CG, Maddox PS, Wang PJ, Adams IR, Salmon ED, Bloom K, Huffaker TC. Control of microtubule dynamics by Stu2p is essential for spindle orientation and metaphase chromosome alignment in yeast. *Mol Biol Cell* 2001;12:2870–2880.
20. Schwartz K, Richards K, Botstein D. BIM1 encodes a microtubule-binding protein in yeast. *Mol Biol Cell* 1997;8:2677–2691.
21. Berlin V, Styles CA, Fink GR. BIK1, a protein required for microtubule function during mating and mitosis in *Saccharomyces cerevisiae*, colocalizes with tubulin. *J Cell Biol* 1990;111(6 Pt 1):2573–2586.
22. Goedhart J, von Stetten D, Noirclerc-Savoye M, Lemmoussin M, Joosen L, Hink MA, van Weeren L, Gadella TW Jr, Royant A. Structure-guided evolution of cyan fluorescent proteins towards a quantum yield of 93%. *Nat Commun* 2012;3:751.
23. Lam AJ, St-Pierre F, Gong Y, Marshall JD, Cranfill PJ, Baird MA, McKeown MR, Wiedenmann J, Davidson MW, Schnitzer MJ, Tsien RY, Lin MZ. Improving FRET dynamic range with bright green and red fluorescent proteins. *Nat Methods* 2012;9:1005–1012.
24. Nagai T, Ibata K, Park ES, Kubota M, Mikoshiba K, Miyawaki A. A variant of yellow fluorescent protein with fast and efficient maturation for cell-biological applications. *Nat Biotechnol* 2002;20:87–90.
25. Mazumder B, Seshadri V, Fox PL. Translational control by the 3'-UTR: the ends specify the means. *Trends Biochem Sci* 2003;28:91–98.
26. McKinney SA, Murphy CS, Hazelwood KL, Davidson MW, Looger LL. A bright and photostable photoconvertible fluorescent protein. *Nat Methods* 2009;6:131–133.
27. Maddox PS, Bloom KS, Salmon ED. The polarity and dynamics of microtubule assembly in the budding yeast *Saccharomyces cerevisiae*. *Nat Cell Biol* 2000;2:36–41.
28. Vorvis C, Markus SM, Lee WL. Photoactivatable GFP tagging cassettes for protein-tracking studies in the budding yeast *Saccharomyces cerevisiae*. *Yeast* 2008;25:651–659.
29. Knop M, Siegers K, Pereira G, Zachariae W, Winsor B, Nasmyth K, Schiebel E. Epitope tagging of yeast genes using a PCR-based strategy: more tags and improved practical routines. *Yeast* 1999;15(10B):963–972.
30. Gibson DG, Young L, Chuang RY, Venter JC, Hutchison CA 3rd, Smith HO. Enzymatic assembly of DNA molecules up to several hundred kilobases. *Nat Methods* 2009;6:343–345.
31. Goldstein AL, McCusker JH. Three new dominant drug resistance cassettes for gene disruption in *Saccharomyces cerevisiae*. *Yeast* 1999;15:1541–1553.
32. Gibeaux R, Politi AZ, Nedelec F, Antony C, Knop M. Spindle pole body-anchored Kar3 drives the nucleus along microtubules from another nucleus in preparation for nuclear fusion during yeast karyogamy. *Genes Dev* 2013;27:335–349.
33. Moore JK, D'Silva S, Miller RK. The CLIP-170 homologue Bik1p promotes the phosphorylation and asymmetric localization of Kar9p. *Mol Biol Cell* 2006;17:178–191.
34. Moore JK, Miller RK. The cyclin-dependent kinase Cdc28p regulates multiple aspects of Kar9p function in yeast. *Mol Biol Cell* 2007;18:1187–1202.
35. Lee WL, Kaiser MA, Cooper JA. The offloading model for dynein function: differential function of motor subunits. *J Cell Biol* 2005;168:201–207.
36. Zaichick SV, Metodiev MV, Nelson SA, Durbrowskyi O, Draper E, Cooper JA, Stone DE. The mating-specific Galpha interacts with a kinesin-14 and regulates pheromone-induced nuclear migration in budding yeast. *Mol Biol Cell* 2009;20:2820–2830.
37. Moore JK, Chudalayandi P, Heil-Chapdelaine RA, Cooper JA. The spindle position checkpoint is coordinated by the Elm1 kinase. *J Cell Biol* 2010;191:493–503.
38. Haarer BK, Helfant AH, Nelson SA, Cooper JA, Amberg DC. Stable preanaphase spindle positioning requires Bud6p and an apparent interaction between the spindle pole bodies and the neck. *Eukaryot Cell* 2007;6:797–807.
39. Song S, Lee KS. A novel function of *Saccharomyces cerevisiae* CDC5 in cytokinesis. *J Cell Biol* 2001;152:451–469.
40. Markus SM, Punch JJ, Lee WL. Motor- and tail-dependent targeting of dynein to microtubule plus ends and the cell cortex. *Curr Biol* 2009;19:196–205.